AGU PUBLICATIONS

Paleoceanography

RESEARCH ARTICLE
10.1002/2016PA003077

Combined Effects of Atmospheric and Seafloor Iron Fluxes to the Glacial Ocean

Juan Muglia[1], **Christopher J. Somes**[2], **Levin Nickelsen**[2], **and Andreas Schmittner**[1]

[1]College of Earth, Ocean and Atmospheric Sciences, Oregon State University, Corvallis, OR, USA, [2]GEOMAR Helmholtz Centre for Ocean Research Kiel, Kiel, Germany

Key Points:
- Effects from dust, sedimentary, and hydrothermal fluxes on glacial iron and carbon are explored
- Higher dust iron flux may have been opposed by reduced sedimentary iron flux due to sea level drop
- The impact on CO_2 is uncertain, ranging from +15 to −28 ppm depending on the mechanisms considered

Correspondence to:
J. Muglia,
jmuglia@coas.oregonstate.edu

Citation:
Muglia, J., Somes, C., Nickelsen, L., & Schmittner, A. (2017). Combined effects of atmospheric and seafloor iron fluxes to the glacial ocean. *Paleoceanography*, *32*, 1204–1218. https://doi.org/10.1002/2016PA003077

Received 19 DEC 2016
Accepted 1 OCT 2017
Accepted article online 5 OCT 2017
Published online 11 NOV 2017

Abstract Changes in the ocean iron cycle could help explain the low atmospheric CO_2 during the Last Glacial Maximum (LGM). Previous modeling studies have mostly considered changes in aeolian iron fluxes, although it is known that sedimentary and hydrothermal fluxes are important iron sources for today's ocean. Here we explore effects of preindustrial-to-LGM changes in atmospheric dust, sedimentary, and hydrothermal fluxes on the ocean's iron and carbon cycles in a global coupled biogeochemical-circulation model. Considering variable atmospheric iron solubility decreases LGM surface soluble iron fluxes compared with assuming constant solubility. This limits potential increases in productivity and export production due to surface iron fertilization, lowering atmospheric CO_2 by only 4 ppm. The effect is countered by a decrease in sedimentary flux due to lower sea level, which increases CO_2 by 15 ppm. Assuming a 10 times higher iron dust solubility in the Southern Ocean, combined with changes in sedimentary flux, we obtain an atmospheric CO_2 reduction of 13 ppm. The high uncertainty in the iron fluxes does not allow us to determine the net direction and magnitude of variations in atmospheric CO_2 due to changes in the iron cycle. Our model does not account for changes to iron-binding ligand concentrations that could modify the results. We conclude that when evaluating glacial-interglacial changes in the ocean iron cycle, not only surface but also seafloor fluxes must be taken into account.

Plain Language Summary During cold climate periods such as the Last Glacial Maximum (LGM, approximately 20 thousand years before present), ice sheets occupied most of North America and Europe, producing lower sea level than in modern times, and atmospheric carbon was also lower than today. One mechanism proposed to link low atmospheric carbon to glacial periods is an increase in the sinking of organic carbon from the surface Southern Ocean and its accumulation in deep waters. This could have happened through iron, an important nutrient for phytoplankton production that is mostly missing in that region. If iron levels were higher in the LGM, then more phytoplankton would grow, sequestering carbon from the atmosphere, and sinking it to deep waters as dead matter. In this work we use a climate model to study differences between the iron cycles of preindustrial times and the LGM. We find that an increase of atmospheric dust flux to the ocean raised ocean iron in the LGM's Southern Ocean, increasing productivity and sinking sequestered atmospheric carbon as organic matter. However, we also find that lower sea level in the LGM exposed continental shelves, decreasing the iron flux coming from marine sediments, acting against the other effect.

1. Introduction

During the Last Glacial Maximum (LGM, ~ 21 kyr before present) atmospheric CO_2 was ~ 100 ppm lower than its preindustrial (PI) value (Marcott et al., 2014). It has been suggested that changes in ocean circulation and biogeochemistry, as well as sea ice cover, could be responsible for this difference (Sigman & Boyle, 2000).

An increase in the export of organic matter could have transferred CO_2 from the atmosphere to deep waters in the LGM. Martin (1990) hypothesized that higher surface iron concentrations in the Southern Ocean (SO) would intensify this region's primary productivity, playing an important role in the sequestration of atmospheric carbon. In the present, most of the surface SO has high levels of nutrient species nitrate (NO_3) and phosphate (PO_4) (Levitus et al., 2013), but low concentrations of dissolved iron (DFe), resulting in low primary productivity and the largest high nutrient low chlorophyll (HNLC) region in the global ocean.

©2017. American Geophysical Union. All Rights Reserved.

Observations and models indicate that LGM atmospheric dust fluxes to the east of Patagonia and into the SO were orders of magnitude higher than in PI times (Lambert et al., 2015; Albani et al., 2014; Maher et al., 2010). Measurements of soluble iron content in LGM dust of Antarctic ice cores also indicate a much higher input than in modern times (Conway et al., 2015). Along with higher dust flux, $^{15}N/^{14}N$ ratios from planktonic foraminifera in SO sediment cores have been interpreted as higher productivity and more efficient nutrient utilization in the LGM compared to the PI (Martínez-García et al., 2014). Meanwhile, Middleton et al. (2016) and Lund et al. (2016) proposed that hydrothermal flux may have been higher during the LGM due to lower water column pressure on hydrothermal vents.

Numerous modeling efforts have studied effects of iron fertilization on the LGM carbon cycle. SO experiments in one-dimensional (vertical) ecological models with increased iron concentrations produce higher export production (Fennel et al., 2003; Mongin et al., 2007). Three-dimensional global ocean models have shown increased export production and atmospheric CO_2 drawdown when applying LGM atmospheric dust fluxes: Bopp et al. (2003) reported an atmospheric CO_2 decrease of up to 30 ppm. Brovkin et al. (2007) obtained a higher number 35 ppm, but their model lacks an iron cycle and they assumed full PO_4 utilization in the Atlantic and Indian sectors of the SO instead. More realistic models that include a representation of iron-binding ligands, which buffer effects of changes in external sources on DFe concentrations (Parekh et al., 2004), estimate a weaker effect of 10–25 ppm (Lambert et al., 2015; Nickelsen & Oschlies, 2015; Parekh et al., 2008; Tagliabue et al., 2009).

Most modeling studies that have simulated the LGM iron cycle have focused on atmospheric flux changes. They assumed constant iron solubility in dust, which could result in overestimations of glacial soluble iron fertilization, since dust concentrations are thought to be inversely proportional to iron solubility (Luo et al., 2008). Sedimentary and hydrothermal iron fluxes have also been proven to affect DFe concentrations in the modern ocean and could drive changes in atmospheric CO_2 (Tagliabue et al., 2010).

Here we study the response of the LGM ocean's coupled iron-biogeochemical system to changes in external iron fluxes and possible impacts on the carbon cycle. We use a three-dimensional global circulation model, coupled with a biogeochemical model that includes a prognostic iron cycle. Changes in the iron inputs to the ocean include dust deposition considering variable iron solubility, sedimentary, and hydrothermal fluxes. Our knowledge of these fluxes has high levels of uncertainty: Atmospheric flux depends on the solubility of iron in dust (Sholkovitz et al., 2012), sedimentary release measurements are limited to a few locations at continental shelves (Elrod et al., 2004), and hydrothermal fluxes are parametrized from ^3He fluxes (Tagliabue et al., 2010). This makes past estimates even more uncertain, so our results should be treated as early speculations of potential glacial-interglacial changes in the iron cycle.

2. Methods

2.1. Physical Model

We use the global ocean circulation model from the University of Victoria (UVic) (Weaver et al., 2001), version 2.9. It consists of a three-dimensional dynamical ocean with 19 vertical levels at 3.6° × 1.8° horizontal resolution governed by the primitive equations, coupled to a two-dimensional single-level atmosphere, with moisture and heat balances and fluxes between the two mediums, and a dynamical sea ice model. It is coupled to a dynamic land vegetation model (Meissner et al., 2003). Winds and clouds are prescribed from present-day monthly climatologies (Kalnay et al., 1996). Background vertical diffusivity was set to 3.5×10^{-5} m^2/s. Our diapycnal mixing scheme includes a three-dimensional parametrization of tide effects (Schmittner & Egbert, 2013). Isopycnal eddy diffusivity was set to 1.2×10^3 m^2/s. Higher values are applied in the tropics, as recommended by Getzlaff and Dietze (2013).

LGM runs use an atmospheric CO_2 value of 185 ppm and orbital parameters from 21 kyr. For continental ice sheets, we use the reconstruction from the Paleoclimate Model Intercomparison Project Phase 3 (PMIP3) setup (Abe-Ouchi et al., 2015). We apply a global 1 PSU addition to salinity to account for sea level drop. A multimodel mean of LGM-PI wind stress anomalies from PMIP3 models was added to the PI wind stress fields. We use PI river routings. The model's circulation with this LGM configuration is described in Muglia and Schmittner (2015).

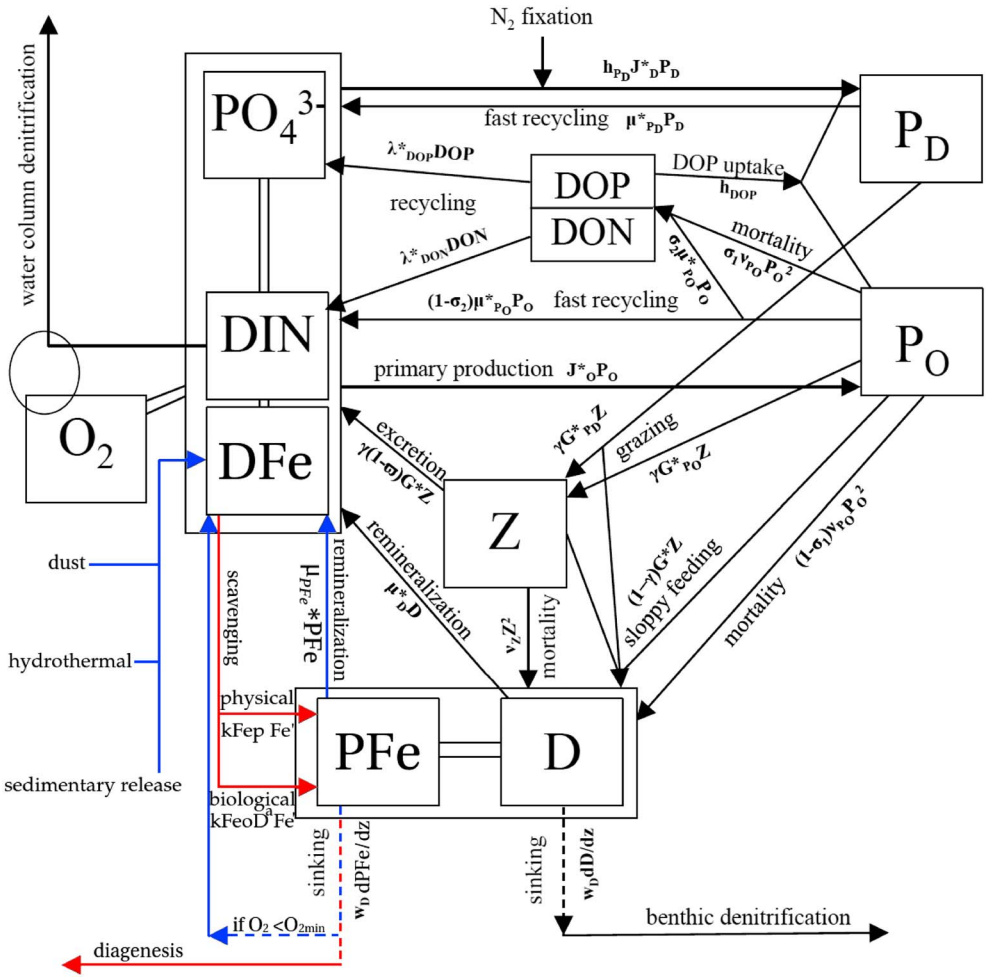

Figure 1. Diagram of our NPZD model. DFe sinks (sources) are highlighted in red (blue).

2.2. Model of Ocean Biogeochemistry

UVic is coupled with the Model of Ocean Biogeochemistry and Isotopes (MOBI), version 1.8, based on Somes and Oschlies (2015), with the implementation of an interactive iron cycle from Nickelsen et al. (2015). It includes prognostic equations for PO_4, NO_3, DFe, O_2, DIC, dissolved organic matter (DOM), particulate organic matter (detritus), PFe, phytoplankton, zooplankton, and diazotrophs (Figure 1). It is embedded within the circulation model, so tracers depend on ocean physics as well as biogeochemical interactions. The phosphorous content of the ocean is assumed constant, but the N cycle includes N_2 fixation by diazotrophs (source of NO_3), and water column and benthic denitrification (sinks of NO_3).

The iron cycle includes external inputs from atmospheric dust, sedimentary, and hydrothermal fluxes. Atmospheric flux is calculated from a prescribed dust flux climatology and added to DFe at the surface. Sedimentary release is proportional to the flux of organic matter reaching the ocean floor. Bulk hydrothermal iron fluxes at mid-ocean ridges were obtained from Tagliabue et al. (2014), regridded to the UVic's grid and multiplied by a factor to preserve the globally integrated flux of the original reconstruction. They are added locally to DFe concentrations at the corresponding grid boxes.

DFe can be scavenged to PFe in the water column and be exported to the sediments where it is either lost or rereleased if the environment is reducing. A step function of O_2 with limit at $O_2 = 5$ μM controls the latter process. Biological and physical scavenging are represented, and depend on a constant iron-binding ligand concentration. Scavenging is proportional to unbound iron. Because ligands reduce unbound iron concentrations, scavenging is lower with higher ligand concentrations. The global constant ligand concentration is 1.5 μmol/m^3, in line with recent simulations with a model that includes ligands as an interactive variable (Völker & Tagliabue, 2015).

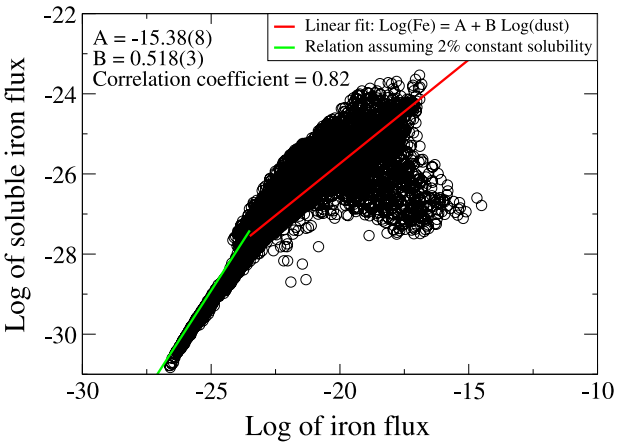

Figure 2. Plot of natural logarithm of atmospheric iron flux versus natural logarithm of soluble iron flux in gFe/(m^2s) units, calculated by an atmospheric model (Luo et al., 2008). The functional form between the two variables represents iron solubility. High values of iron flux are fitted by a power law (red line). For low values we use a constant 2% solubility (green line).

Biological and inorganic scavenging rates have been increased from 0.45 (m^3/(gC d))$^{0.58}$ and 0.005 d^{-1} in Nickelsen et al. (2015) to 1.0 (m^3/(gC d))$^{0.58}$ and 0.016 d^{-1}, respectively, to equilibrate at observed iron concentrations due to the addition of hydrothermal flux to the model. The iron maximum half saturation constant for phytoplankton growth has been decreased, from 0.4 µmol Fe/m^3 in Nickelsen et al. (2015) to 0.2 µmol Fe/m^3, to better represent surface SO PO_4 and NO_3 concentrations. All other biogeochemical parameters have been kept as in Nickelsen et al. (2015) (for iron variables) and Somes and Oschlies (2015) (for other biogeochemical variables).

Due to the scarcity and variability of observations (Tagliabue et al., 2012), the dynamism of its fluxes (Tagliabue et al., 2014) and the complex interactions among its components, current model representations of the iron cycle, including this one, have high uncertainties and biases (Tagliabue et al., 2016). Although our model includes a constant parameter to represent iron-binding ligands, an interactive cycle could be a more realistic approach. However, the high complexity of ligand chemistry and distributions, with different species in different sectors of the ocean (Gledhill & Buck, 2012), could bring additional uncertainties to our LGM estimates. Here we focus on direct effects of changes in the iron fluxes, subject to the assumption of constant ligand concentrations.

2.3. Iron From Dust Flux

PI and LGM surface soluble iron fluxes were generated from interpolated dust flux monthly climatologies from these two time periods (Lambert et al., 2015). We assume a 3.5% iron content in dust (Mahowald et al., 2009).

Luo et al. (2008) used an atmospheric model to generate fields of modern dust flux, soluble iron flux, and solubility of iron in dust. They estimated higher solubility with lower dust concentration. To calculate iron solubility for our dust fields, we created a scatterplot of soluble iron versus iron in dust from a preindustrial realization from Luo et al. (2008), and fitted a curve to it (Figure 2). A constant 2% (as assumed in Lambert et al., 2015) solubility provides a good fit for low dust concentrations, but a power law is more accurate at higher values. Our solubility fit is a piecewise function of these two curves, and it was applied to dust fluxes from Lambert et al. (2015), transforming them into monthly climatologies of soluble iron flux. Solubilities range between 0.02% and 2.0%, with PI and LGM global means of 0.8% and 0.4%, respectively. Due to the lower solubility, surface iron flux must be more than twice its PI value in order to have glacial iron fertilization. Dust deposited above sea ice cannot reach surface waters, so in grid boxes with sea ice fraction we decreased iron flux by a percentage equal to that fraction. Iron is accumulated in these ice covered grid boxes and released when sea ice melts.

Our estimated LGM surface soluble iron fluxes are higher than PI in parts of the SO, to the east of the Patagonian region and around continents (Figure 3). Modern measurements of atmospheric dust concentrations and solubility have high uncertainties (Sholkovitz et al., 2012; Winton et al., 2016), so the real LGM surface soluble iron fluxes may have been very different from what we estimate. In order to consider this uncertainty we perform an additional sensitivity experiment where LGM soluble flux is multiplied by 10 south of 35°S. This estimate is in line with measurements from Antarctic ice cores, where LGM soluble iron fluxes were found to be of the order of $\geq$ 10 times larger than PI values (Conway et al., 2015).

2.4. Iron From Sedimentary Release

Sedimentary DFe release is proportional to the flux of organic carbon reaching the bottom of the ocean, with an exponential temperature dependence, to account for temperature-dependent remineralization (Nickelsen et al., 2015). In the real ocean this process is especially relevant over continental shelves (Elrod et al., 2004), but UVic's coarse resolution bathymetry is not able to resolve shallow bottom features. Therefore, we use a subgrid bathymetry function that specifies the fraction of ocean bottom at each ocean grid box and is multiplied to the sedimentary release. For each grid box at position i, j, k, the subgrid bathymetry parameter $sgb(i, j, k)$ is defined as

$$sgb(i,j,k) = \begin{cases} f(i,j,k) & \text{if } k = 1(\text{surface}) \\ \frac{f(i,j,k)}{1-\sum_{n=1}^{k-1} f(i,j,n)} & \text{otherwise,} \end{cases} \quad (1)$$

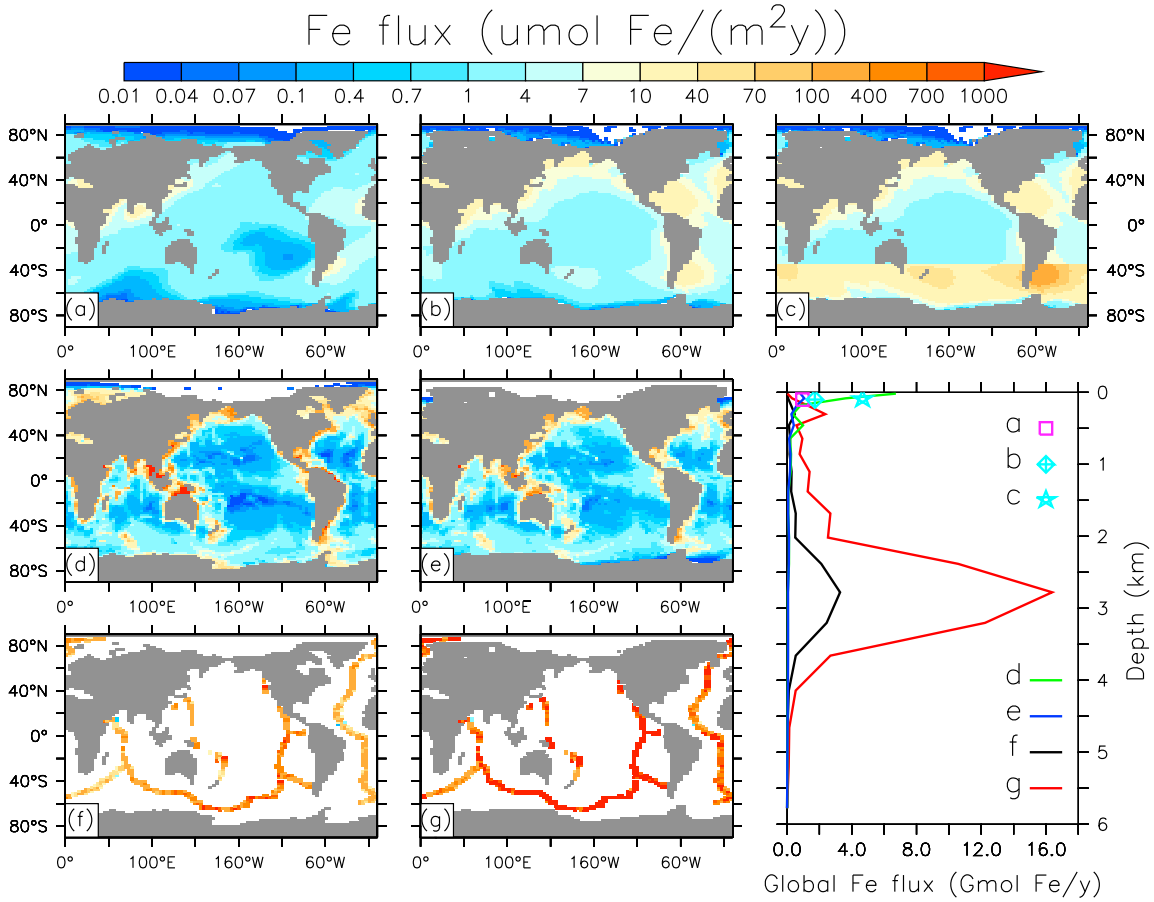

Figure 3. Soluble iron fluxes used in the model. Top surface maps are surface atmospheric fluxes corresponding to (a) PI, (b) LGM, and (c) LGM with 10 times deposition in the SO. Middle surface maps are sedimentary fluxes for (d) PI, and (e) LGM (LGM_Fe simulation). Bottom maps are hydrothermal fluxes, corresponding to (f) PI and (g) 5×PI. The color scale is logarithmic. The depth profile plot shows the same fluxes, as indicated by the letter codes, integrated horizontally and over the thickness of each of the model's vertical levels. Atmospheric fluxes only have values at the surface.

where $f(i,j,k)$ is the fraction (from 0 to 1) of ocean bottom at each grid box. Fractions were calculated using the ETOPO 2 min resolution bathymetry (National Geophysical Data Center, 2006).

At each grid box, imported detritus is remineralized into PO_4 and NO_3 in a fraction equal to $sgb(i,j,k)$. Benthic denitrification is also proportional to $sgb(i,j,k)$ (Somes & Oschlies, 2015). $sgb(i,j,k)$ is defined so that no vertical fluxes penetrate the subgrid defined ocean bottom, and no benthic denitrification or DFe sedimentary release occurs beyond this depth. Any detritus left at the resolved-bathymetry ocean bottom is automatically remineralized.

LGM sedimentary fluxes were calculated taking into account sea level changes. We considered a 125 m lower sea level (Lambeck et al., 2014) when calculating the subgrid bathymetry (ocean volume remained unchanged), obtaining lower or zero ocean bottom fractions over continental shelves and higher values in deeper, offshore grid boxes. This results in lower sedimentary fluxes around continents and higher fluxes in deep waters (Figure 3). We left the model's resolved bathymetry unchanged, so the effect of lower sea level on DFe fluxes is possibly underestimated. The sea level lowering in our simulations did not affect the global mean phosphate concentration.

2.5. Iron From Hydrothermal Fluxes

PI hydrothermal fluxes were obtained from Tagliabue et al. (2014). Recently, a sediment core from the mid-Atlantic Ridge provided evidence that due to lower sea level and bottom pressure, past hydrothermal iron fluxes may have been up to 8 times higher than today (Middleton et al., 2016). We thus produce an LGM simulation where hydrothermal iron fluxes are increased fivefold from their PI values (Figure 3).

Table 1
Experiment List

Experiment name	Boundary conditions	Surface Fe deposition	Subgrid bathymetry	Hydrothermal Fe
PI_control	PI	PI	PI	×1
LGM_default	LGM	PI	PI	×1
LGM_sed	LGM	PI	LGM	×1
LGM_dust	LGM	LGM	PI	×1
LGM_Fe	LGM	LGM	LGM	×1
LGM_hydro	LGM	LGM	LGM	×5
LGM_highFe	LGM	LGM high	LGM	×1

Note. Boundary conditions, surface iron deposition, subgrid bathymetry, and multiplying factor of hydrothermal iron input are specified. LGM high refers to LGM surface iron deposition with 10 times factor in the SO.

2.6. Experiments

In Table 1 we describe our full array of experiments. PI_control is a default PI run. LGM_default uses LGM boundary conditions as described in section 2.1 but uses PI iron inputs. LGM_sed and LGM_dust are like LGM_default but with LGM sediment and surface soluble iron fluxes, respectively. LGM_Fe combines both modifications. LGM_hydro is like LGM_Fe but with the addition of extra hydrothermal iron. LGM_highFe uses higher LGM surface iron fluxes in the SO as described in section 2.3. Each experiment was run for 6 ky from PI conditions, and results from the last 500 years are shown, with a drift in global tracers lower than 0.1% through that period.

3. Results

3.1. Modern Biogeochemistry

Distributions of DIC, PO_4, and NO_3 are generally well represented in our PI control simulations, with correlations to modern observations higher than 0.9, similar to previous versions (Somes & Oschlies, 2015).

PI DFe fields fail to reproduce the high variability in the deep ocean of observations compiled by GEOTRACES (Tagliabue et al., 2012, updated to its 2015 version). Our model result produces smooth fields, and its standard deviation is 1 order of magnitude smaller than that of the observations, which appear noisy (Figure 4). This produces low correlation coefficients in most depth sections when compared to observations (Table 2). The GEOTRACES iron data have a temporal sampling bias, with more measurements taken in summer months in each hemisphere, and a time span of 20 years that includes high interannual differences (Tagliabue et al., 2012). Our equilibrium simulation does not capture other temporal variability than the seasonal cycle, and we compare the data to the annual mean of model results, which contributes to model data mismatches. If we only include data points inside the $\pm$ two standard deviations from the mean (DFe $\leq$3.11 nM, data points decrease from 18,440 to 18,196) the correlations are improved, illustrating that data outliers are a significant cause for the disagreement. Root-mean-square error (RMSE) and model data biases are higher in this case, due to an overestimation in the model's ocean's interior DFe concentrations, which produces modeled means to be closer to observations when higher values are not removed from the data set.

The model overestimates the deep DFe global mean by up to 25%, probably due to too little scavenging to counter the high DFe additions from hydrothermal sources. It is possible that the stability constant that we use for the chemical equilibrium of ligand-bound iron, free ligands, and free iron is too high for deep waters, since our value has been reported for the upper ocean, while lower values exist elsewhere. This would shift the equilibrium too much toward the ligand-bound iron state, resulting in too little scavenging in deep waters (Gledhill & Buck, 2012).

GEOTRACES zonally averaged sections of DFe show deep localized maxima that are not well reproduced in the ocean biochemistry model (Figure 4). Some middepth maxima are associated with hydrothermal iron release, which according to recent observations has a very distinguishable signal, like in the South Pacific where DFe is transported for longer distances than previously thought, and a far-reaching plume is observed (Resing et al., 2015). Our model at that location exhibits a lower DFe zonal gradient, with values away from the hydrothermal plume higher than the observations. This is probably caused by too low deep scavenging that imposes that

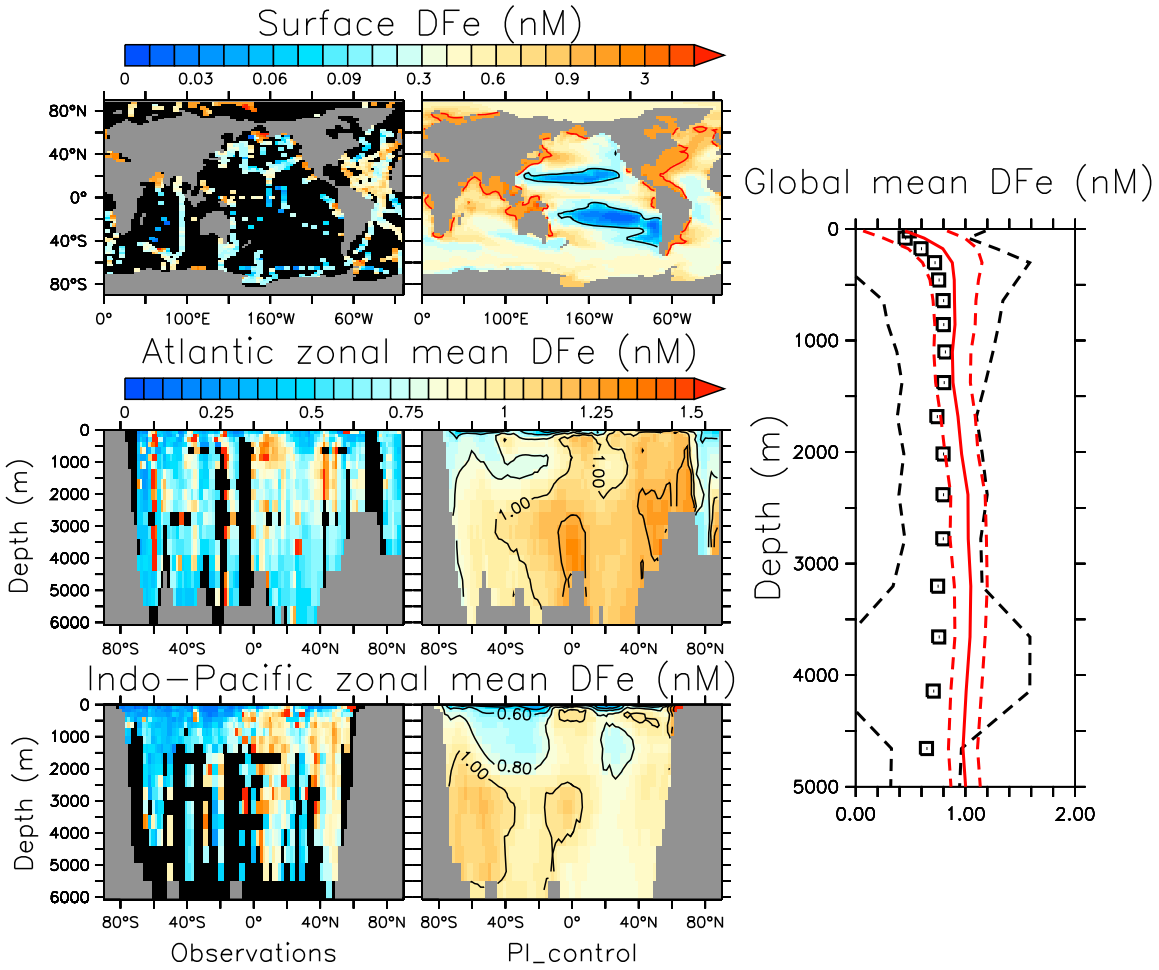

Figure 4. (top left) Surface DFe from modern GEOTRACES observations and PI_control. Black (red) contours are the 0.1 (1) nM isolines. Color scale is logarithmic. (middle and bottom left) Zonally averaged DFe concentrations versus latitude from modern GEOTRACES observations and PI_control, for the Atlantic and Indo-Pacific oceans. (rightmost panel) Global mean DFe versus depth (black squares) from observations and (red line) PI_control, averaged over locations where observations exist. Black (red) dashed lines show the ± standard deviations of the observations (model).

too much hydrothermal iron is mixed in the water column before being transformed into PFe, resulting in a more homogeneous distribution and higher background values than the observations.

The model surface mean has a lower bias with respect to observations than other sectors (Table 2 and Figure 4). At the surface, modeled DFe is overestimated in HNLC regions and in continental margins, similar to Nickelsen et al. (2015). These differences could be due to biases in the DFe fluxes or the absence of diatoms as a separate type of phytoplankton in the model that would increase iron consumption at high concentrations. Low DFe concentrations are well reproduced in the Pacific Ocean, as well as high values in some parts of the Atlantic.

Table 2
Comparison of PI_Control Versus Observations From GEOTRACES (Tagliabue et al., 2012), for the Same Depth Sections of Tagliabue et al. (2016)

Parameter	Global	0–100	100–500	500–1,000	2,000–5,000
R	0.25/0.36	0.22/0.25	0.23/0.39	0.33/0.44	0.17/0.25
RMSE	1.05/1.14	1.09/1.24	1.03/1.13	0.97/0.98	1.16/1.43
Bias (nM)	0.26/0.29	0.07/0.12	0.17/0.23	0.11/0.14	0.28/0.31

Note. DFe correlation coefficient, standard deviation-normalized root-mean-square Error (unitless), and model-observation bias. Values obtained comparing to all GEOTRACES data points/only data inside the $\pm 2\sigma$ confidence bar.

Table 3
DFe Global and Surface (0–120 m) Contents (in Tg Fe Units), and Surface, Hydrothermal, Sedimentary, PFe Remineralization, and Scavenging Fluxes (in Tg Fe/y Units) From Our Model Simulations

	Global content	Surface content	Surface flux	Hydrothermal flux	Sedimentary flux	Remineralization flux	Scavenging flux
PI_control	68.920	1.050	0.05	0.63	0.77	5.60	5.14
LGM_default	63.760	0.915	0.05	0.63	0.51	4.00	3.76
LGM_sed	56.980	0.542	0.05	0.63	0.22	2.52	2.47
LGM_dust	65.400	1.046	0.10	0.63	0.45	4.10	3.94
LGM_Fe	59.820	0.686	0.10	0.63	0.24	2.80	2.72
LGM_hydro	71.34	0.795	0.10	3.20	0.25	5.90	8.00
LGM_highFe	67.340	1.078	0.26	0.63	0.23	3.40	3.48

Compared to the set of ocean iron models presented in Tagliabue et al. (2016), MOBI has lower correlation coefficient to observations than most of them, especially at the surface. Its global mean bias is similar to the other models. Some of the differences between other iron models and ours may lie in the sources. Our total deep iron flux (sedimentary + hydrothermal, Table 3) is higher than in all but two of the models from Tagliabue et al. (2016), and the contribution from atmospheric fluxes is smaller in MOBI (3.5%) relative to models presented in that review (21 to 87%). This, together with the lack of enough scavenging, probably results in the positive bias that we obtain through most of the water column and likely increases the relative importance of nonaeolian fluxes in our model. Poor knowledge hinders our ability to properly constrain DFe fluxes, although we acknowledge that MOBI has room for improvement, and detailed aspects of the results should therefore be viewed with caution.

3.2. The LGM Iron Cycle

Colder water temperatures in LGM_default with respect to PI_control produce a 34% decrease in DFe sedimentary release due to its temperature dependence (equation (25) in Nickelsen et al., 2015) and 19% decrease in detrital remineralization rate (Table 3), resulting in lower ocean DFe.

Lower sea level tends to reduce surface DFe, especially where continental shelves become exposed and no longer contribute to sedimentary flux. A glacial simulation with LGM subgrid bathymetry (LGM_sed) produces surface DFe values lower than those obtained in LGM_default (Figure 5). DFe sedimentary flux decreases by 57% globally and surface concentrations by 41% compared with LGM_default, and by 71% and 48%, respectively, compared with PI_control.(Table 3).

Applying LGM atmospheric soluble iron deposition (LGM_dust) has the opposite effect and leads to a modest increase in global surface DFe. Most of the increase occurs in the subtropics, in the North Atlantic, and in the Arctic, whereas the impact is minimal in the SO, southern Indian, and tropical Pacific. The differences in surface DFe among experiments are persistent throughout the water column, illustrating efficient downward transport through scavenging (Figure 5).

Adding both effects together (LGM_Fe) we obtain higher surface DFe values in some regions, but the effect of lower sedimentary release dominates in most of the ocean. The extra increase in SO LGM surface flux of LGM_highFe surpasses the sea level effect in that region and produces high DFe, especially in the 30° − 50°S band, where surface values are up to 20 times higher than in LGM_default (Figure 5).

Multiplying the hydrothermal source of DFe by 5 (LGM_hydro), although globally a much larger addition than LGM_highFe, produces a relatively smaller effect on surface concentrations. However, the 15% increase in SO export production between LGM_hydro and LGM_Fe (Table 4) shows that there is some amount of control of hydrothermal DFe on primary productivity, as suggested by recent measurements and simulations by Resing et al. (2015).

High concentrations of DFe are always accompanied by high scavenging and water column PFe remineralization (Table 3). If the extra iron input comes from deep sources, then DFe scavenging prevents it from producing surface iron fertilization. The increase in scavenging due to the addition of extra atmospheric dust is more modest, allowing surface values to increase more.

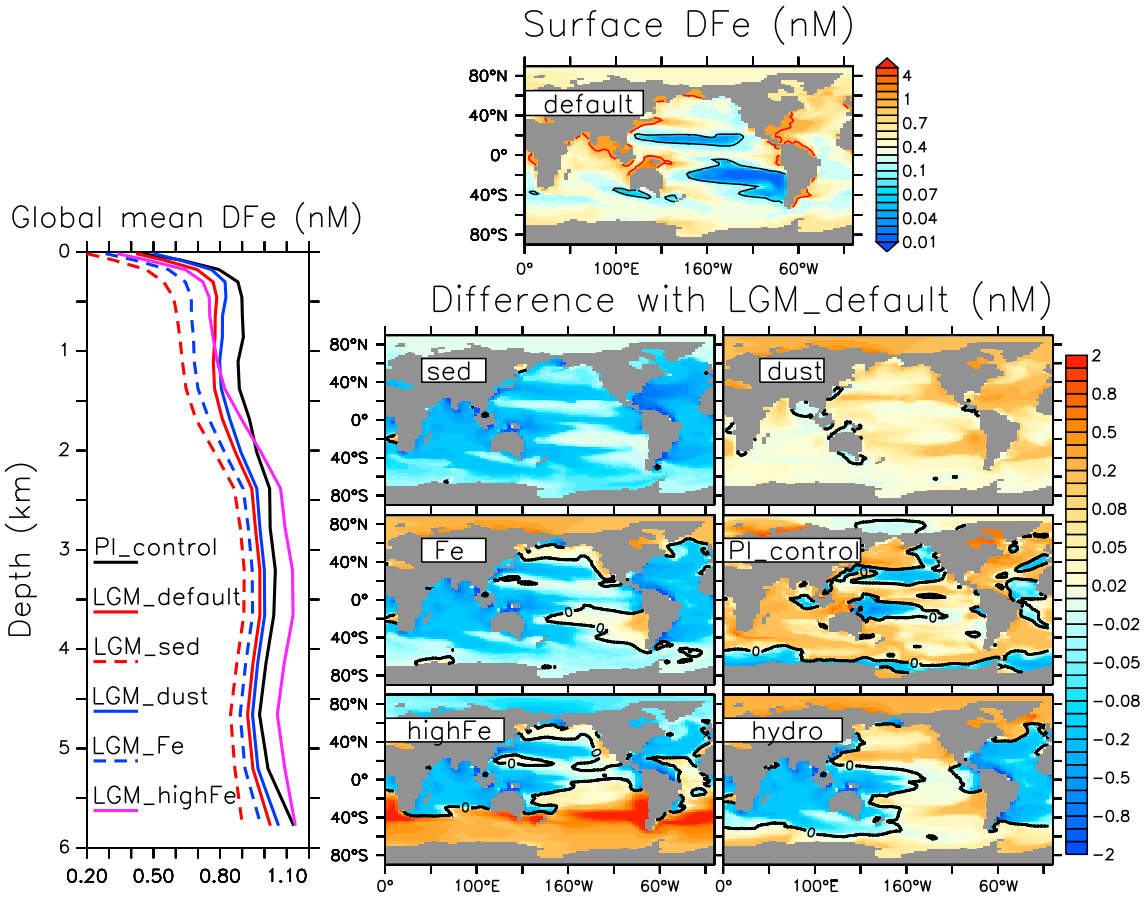

Figure 5. (top) Surface DFe from LGM_default. Isolines as in Figure 4. (bottom right six panels) Surface DFe differences between our experiments and LGM_default. xxx labels refer to the LGM_xxx experiment listed in Table 1 except for PI_control. Color scales are logarithmic. (left) Global mean DFe versus depth for some of our experiments. LGM_hydro values lay beyond the scale of the plot.

3.3. Effects on the LGM Carbon Cycle

Our modeled LGM ocean has lower mean DIC than PI_control (Table 4). The reasons are the constant atmospheric CO_2 boundary condition that we use, which in the LGM forces the ocean to equilibrate to a lower value than in the PI, and the lack of a sediment model that would enable changes in ocean alkalinity (Schmittner & Somes, 2016).

The ocean carbon cycle is affected by changes in iron inputs via primary productivity and export of organic matter to deep waters. Experiments with higher phytoplankton concentrations have higher export production and DIC, indicating an increased efficiency of the biological pump. Isolating the global effects of extra

Table 4
Simulations' SO (90°–40°S)/Global Phytoplankton Content and Export Production Out of the Euphotic Zone (Calculated as the Downward Export of Detritus at 120 m), Global Detritus Remineralization Below 2,000 m, and Global Content of DIC

	Phytoplankton (Pg C)	Export production (Pg C/y)	Deep detritus remineralization (Pg C/y)	Global DIC (Pg C)
PI_control	0.14(11)/0.66(6)	1.9(2)/8.36(8)	0.33(8)	8333(1)
LGM_default	0.11(8)/0.56(5)	1.5(1)/7.42(6)	0.39(7)	8131(1)
LGM_sed	0.09(7)/0.46(4)	1.17(9)/6.00(5)	0.31(6)	8061(1)
LGM_dust	0.12(9)/0.58(5)	1.6(1)/7.67(6)	0.41(7)	8152(1)
LGM_Fe	0.10(8)/0.51(4)	1.3(1)/6.85(5)	0.36(6)	8106(1)
LGM_hydro	0.11(9)/0.54(5)	1.5(1)/7.24(6)	0.39(7)	8136(1)
LGM_highFe	0.16(13)/0.58(9)	2.2(2)/7.63(10)	0.44(12)	8251(1)

Note. Parentheses standard deviations in the last digit are from seasonal amplitude.

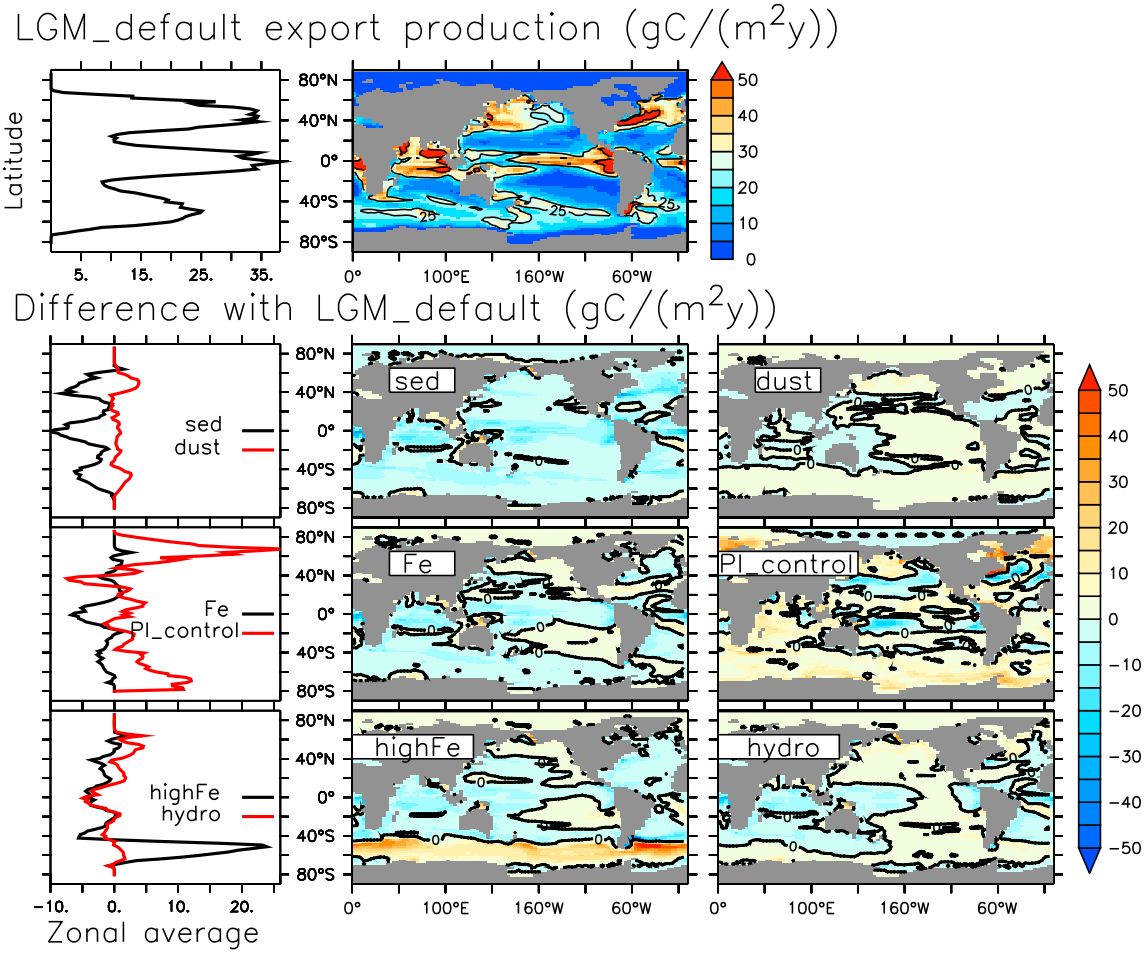

Figure 6. (top panel) LGM_default export production. (bottom panels) Differences between LGM experiments and LGM_default. (left column) Zonal averages versus latitude (with transposed axes) for the experiments shown at each row. Labels as in Figure 5.

DFe in LGM_dust and LGM_hydro by comparing them to LGM_default and LGM_Fe, respectively, shows modest effects on global phytoplankton concentrations and export production (Table 4). However, the decrease in sedimentary flux results in less organic carbon export out of the surface ocean (Figure 6).

In the SO between Antarctica and 60°S, export production is lower in LGM simulations compared to PI_control because of the larger extension of sea ice. North of that, because of the prescribed tenfold increase in SO atmospheric soluble iron flux, LGM_highFe exhibits a conspicuous increase in the band between 60° and 40°S. The maximum increase is from 30 to 70 g C/(m^{2}y), between 45° and 55°S, east of Patagonia (Figure 6) coincidental with high atmospheric iron fertilization. LGM_highFe gives a result in agreement with Kohfeld et al. (2005), whose analysis indicated that LGM export production must have increased north of the Antarctic Polar Front but decreased south of it.

Sections of LGM-PI DIC (Figure 7) show that waters with relatively higher carbon content originate in the upper SO and propagate northward as deep and intermediate waters. As a consequence of atmospheric iron fertilization, LGM_dust and LGM_highFe exhibit the highest organic carbon remineralization rates and global DIC contents (Table 4). In other experiments, the decrease in sedimentary iron release inhibits surface fertilization effects.

The extra hydrothermal deep iron flux in LGM_hydro does not produce a considerable change in DIC compared to LGM_Fe, which has the same setup except for hydrothermal sources (Figure 7). The extra DFe in LGM_hydro is quickly scavenged and contributes less to export production than the higher surface flux of LGM_highFe.

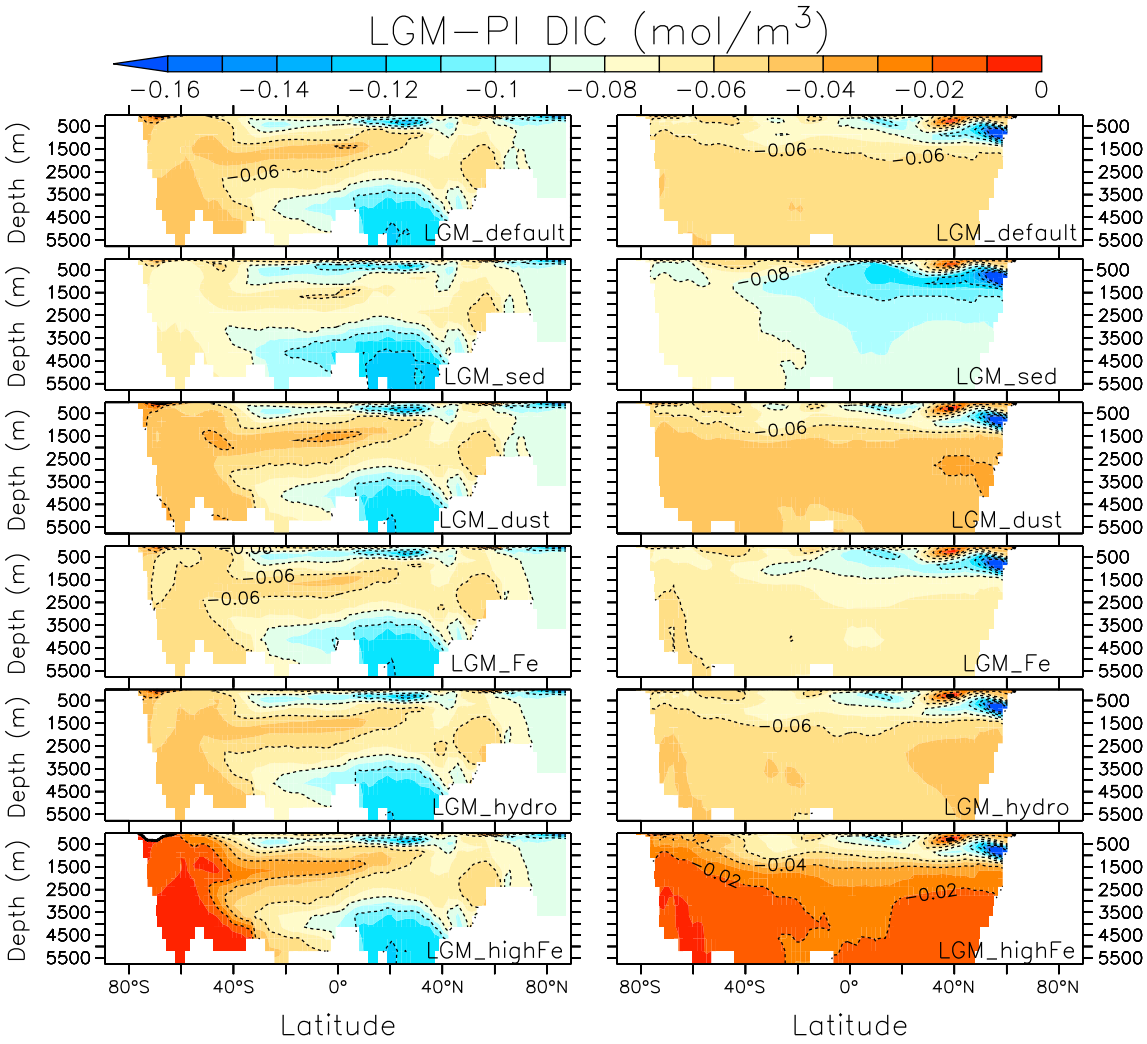

Figure 7. Zonally averaged sections of DIC difference between LGM experiments and PI_control. Plots correspond to the (left column) Atlantic and (right column) Indo-Pacific ocean basin.

The effect of high SO iron fertilization in LGM_highFe is important for the carbon cycle. SO export production out of the euphotic zone is higher than in PI_control (Table 4) and appears to be in better agreement with reconstructions (Martínez-García et al., 2014; Kohfeld et al., 2005). Its global DIC content is considerably higher than in other LGM experiments, as a result of more accumulation of remineralized organic carbon (C_{remi}), the amount of DIC formed by the respiration of organic matter.

For situations where there is no change in the physical characteristics of the ocean, like our LGM experiments, changes in C_{remi} can be calculated from the formula $\Delta C_{remi} = R_{C:O} \times \Delta AOU$, where $R_{C:O}$ is the carbon to oxygen Redfield ratio and AOU is the apparent oxygen utilization. From ΔC_{remi} we can determine an associated change in atmospheric CO_2 (Ito & Follows, 2005):

$$\Delta pCO_2^{atm} = -\frac{V}{M\gamma}\Delta C_{remi}, \tag{2}$$

where $V = 1.358 \times 10^{18}$ m^3 is the volume ocean in our model grid, $M = 1.77 \times 10^{20}$ is the atmosphere's combined gas moles, and

$$\gamma = 1 + \frac{V\bar{C}_{sat}}{BMpCO_2^{atm}}. \tag{3}$$

γ depends on $B = 10$, the buffer factor for sea-air equilibrium of carbon (Ito & Follows, 2005), $\bar{C}_{sat}$, the mean preformed carbon concentration at equilibrium with the atmosphere, and pCO_2^{atm}, which was set to 185 ppm

Table 5
Change in Global Remineralized Carbon and Potential Effect on pCO_2^{atm} Corresponding to the Different LGM-PI Changes in DFe Inputs That We Analyze

Input changed	ΔC_{remi} (Pg C)	Effect on atmospheric CO_2 (ppm)
Dust (LGM_dust - LGM_default)	78	−4
Dust (LGM_Fe - LGM_sed)	174	−9
Sedimentary (LGM_sed-LGM_default)	−279	15
Sedimentary (LGM_Fe-LGM_dust)	−182	10
Sedimentary + dust (LGM_Fe-LGM_default)	−104	5
Hydrothermal (LGM_hydro-LGM_Fe)	118	−6
Dust, higher in SO (LGM_highFe-LGM_sed)	537	−28
Dust, higher in SO + sed. (LGM_highFe-LGM_default)	248	−13

Note. Parentheses specify which experiments we compare to obtain each estimate. Results depends not only on the input changed but also on the pair of experiments that are compared, thus the repetition of dust and sedimentary cases.

in our LGM setup. For LGM_default, $\gamma = 8.98$. The uncertainty in our calculation of ΔpCO_2^{atm} is given by the assumption of an equilibrium state and air-sea equilibrium between preformed carbon and atmospheric CO_2. We calculated the uncertainty associated with the first assumption, obtaining a value of 3.6%.

Isolating the surface iron fertilization effect by comparing LGM_dust to LGM_default, we obtain a decrease in pCO_2^{atm} of 4 ppm (Table 5), about half of what Lambert et al. (2015) obtain from the same dust fields (with constant solubility parametrization, which results in higher SO fertilization than with our variable solubility method). The higher iron fertilization used in LGM_highFe raises this number to 28 ppm, which is close to 25 ppm, from a PI experiment that included a dust flux increase of comparable magnitude to LGM_highFe (Nickelsen & Oschlies, 2015). By comparing LGM_sed with LGM_default we can isolate the effect of changes in LGM sedimentary DFe release on pCO_2^{atm}: A decrease in global C_{remi} produces a raise of 15 ppm. Increasing DFe hydrothermal flux has a 6 ppm negative effect on pCO_2^{atm}, a value similar to changes produced by the default dust case but smaller than the effects of the high dust and sediment cases.

The nonlinearity of the iron cycle brings additional uncertainties to pCO_2^{atm} estimates. Calculating the effect of increased dust and reduced sedimentary release from LGM_Fe-LGM_sed and LGM_Fe-LGM_dust, respectively, gives different values than the ones presented above, with a reduction (amplification) of the sedimentary (atmospheric) effect (Table 5).

Another source of uncertainty is the assumed constant ligand concentration. A PI simulation where the global ligand concentration was decreased from 1.5 to 1 μmol/m^3 (not shown) exhibits higher scavenging and lower DFe, resulting in potentially 5 ppm higher pCO_2^{atm}, in agreement with experiments with a similar iron model (Parekh et al., 2008). For instance, our calculated LGM-PI changes in ocean biogeochemistry and pCO_2^{atm} due to variations in iron fluxes may have been dampened or amplified by the effect of ligands, but our model configuration does not take this effect into account.

4. Discussion

SO surface iron fertilization has been hypothesized as a possible driver for lower atmospheric CO_2 and higher deep ocean DIC during the LGM (e.g., Sigman & Boyle, 2000), which some of our results support. However, because of the possibility of lower sedimentary flux around continents and the high uncertainties of our estimations, a negative effect on DIC from changes in the iron cycle, which translates into a potential increase in pCO_2^{atm}, cannot be ruled out. In LGM_highFe the surface iron fertilization surpasses the sedimentary release effect, resulting in a potential 13 ppm lower pCO_2^{atm} (Table 5), which would be a significant contribution to glacial-interglacial CO_2 changes. Given the uncertainty of LGM dust reconstructions, that results in mismatches of up to 1 order of magnitude between Lambert et al. (2015) and Albani et al. (2014), and the uncertainties in solubility estimates, this remains as a plausible scenario.

Our parametrization of sedimentary release is taken from Galbraith et al. (2010) and is proportional to the organic carbon flux reaching the ocean floor. Dale et al. (2015) proposed a parametrization with DFe release as

a function of organic carbon flux and bottom oxygen levels. They obtained surface iron fields more dependent on sediment fluxes, so their parametrization would presumably have a higher impact on LGM DFe changes.

Rivers have been pointed out to proportionate reactive iron to continental margins, balancing sources and sinks of sedimentary iron. A more realistic representation should include riverine DFe flux independently or as a part of the sedimentary flux (Nickelsen, 2015). Lower sea level in the LGM could have exposed most of modern day estuaries, decreasing the amount of riverine DFe scavenged and providing a new source for iron to the ocean. This and other scenarios are not tested in this work and should be addressed in the future.

For the LGM-PI change in sedimentary release we decreased sea level by 125 m in the calculation of the model's subgrid bathymetry. Conversely, glacial sea level changes were not spatially homogeneous, as isostatic adjustment produces local inhomogeneities in sea level in the presence of ice sheets (Clark et al., 2002). We performed an extra simulation using spatially inhomogeneous subgrid bathymetry calculated from the ICE-6G LGM bottom topography (Peltier et al., 2015) to test the significance of spatially variable sea level changes, finding very little difference compared to when spatially constant effects were accounted.

Our biogeochemical model only includes diazotrophs and general phytoplankton as primary producers. The lack of diatoms and/or a silicate cycle means that we cannot simulate species shifts due to changes in DFe. We have parametrized this effect by using a variable iron half saturation constant that increases proportionally with phytoplankton concentrations. This assumes that at higher iron concentrations we get bigger phytoplankton cells, which in turn require more iron uptake for their metabolism (Nickelsen et al., 2015). We have not included the increase in ballasting associated with such shifts from light to heavier cells, so we might be underestimating changes in SO export production.

Another possible limitation of our model is its coarse resolution. In the modern ocean iron fertilization can cause primary productivity to increase considerably in continental margins and around islands (Moore et al., 2000). Such mesoscale features are not captured in our simulations, and instead we have an open ocean, less intensified effect. The coarse resolution may also cause underestimations of sedimentary flux over narrow shelves or other steep but otherwise small features that are not well defined by our subgrid bathymetry parameter (Somes et al., 2017).

Iron-binding ligands are an important component of the ocean iron cycle and limit DFe scavenging. Their concentration was kept constant, so we do not address effects of variations in ligand concentrations due to changes in iron fluxes or from glacial/interglacial conditions. Our choice of leaving ligand concentrations constant is based on the uncertainty in the LGM-PI direction of change of the numerous factors affecting them (Völker & Tagliabue, 2015). Changes in ligands could be as important as iron fluxes and should be taken into account in future studies (Parekh et al., 2008).

Our work does not explicitly consider other processes that could have produced glacial-interglacial changes in the carbon cycle. Changes in ocean circulation (Brovkin et al., 2007), stratification (Franois et al., 1997), phosphorous burial (Palastanga et al., 2013), and nitrate fluxes (Somes et al., 2017) have been pointed out to affect the LGM's ocean biogeochemistry and carbon. Our analysis suggests that when evaluating the effect of changes in the ocean iron cycle on glacial-interglacial atmospheric CO_2 variations, it is necessary to take into account sedimentary and hydrothermal fluxes, as well as surface fluxes. This result is in line with the recent realization of the importance of iron sources other than dust (Tagliabue et al., 2017). The limitations of our model do not allow us to robustly estimate the direction and magnitude of CO_2 variations due to glacial-interglacial changes in the iron cycle.

5. Conclusions

We have performed sensitivity experiments with an ocean biogeochemical model that includes iron as one of its interactive nutrients, to test the significance of iron changes in glacial-interglacial variations of the carbon cycle. Our results are consistent with prior works that show that higher dust deposition in the LGM lowered atmospheric CO_2, but a reduction of sedimentary flux due to a simple assumption regarding sea level control has the opposite tendency and could have a similar magnitude. If LGM SO soluble iron deposition is ≥ 10 its PI values, then the lower sedimentary release is overcompensated in our model, and atmospheric CO_2 is reduced by 13 ppm. Note that changes in ligand concentrations are not addressed in this work.

Our study suggests that all important iron fluxes should be considered to accurately quantify the net effect of glacial-interglacial atmospheric CO_2. The high uncertainty in our knowledge of the iron cycle does not allow robust estimates of the direction and magnitude of this net effect.

Acknowledgments
This study was supported by NSF's Marine Geology and Geophysics program (OCE-1131834 and OCE-1235544). C. S. was supported by the SFB 754 project from the Deutsche Forschungsgemeinschaft. Model results are available at NOAA's paleoclimate repository (https://www.ncdc.noaa.gov/paleo-search/study/21331).

References

Abe-Ouchi, A., Saito, F., Kageyama, M., Braconnot, P., Harrison, S., Lambeck, K., … Takahashi, K. (2015). Ice-sheet configuration in the CMIP5/PMIP3 Last Glacial Maximum experiments. *Geoscientific Model Development*, *8*(6), 3621–3637.

Albani, S., Mahowald, N., Perry, A., Scanza, R., Zender, C., Heavens, N., … Otto-Bliesner, B. (2014). Improved dust representation in the Community Atmosphere Model. *Journal of Advances in Modeling Earth Systems*, *6*, 541–570. https://doi.org/10.1002/2013MS000279

Bopp, L., Kohfeld, K. E., Le Quéré, C., & Aumont, O. (2003). Dust impact on marine biota and atmospheric CO_2 during glacial periods. *Paleoceanography*, *18*(2), 1046. https://doi.org/10.1029/2002PA000810

Brovkin, V., Ganopolski, A., Archer, D., & Rahmstorf, S. (2007). Lowering of glacial atmospheric CO_2 in response to changes in oceanic circulation and marine biogeochemistry. *Paleoceanography*, *22*, PA4202. https://doi.org/10.1029/2006PA001380

Clark, P. U., Mitrovica, J., Milne, G., & Tamisiea, M. (2002). Sea-level fingerprinting as a direct test for the source of global meltwater pulse IA. *Science*, *295*(5564), 2438–2441.

Conway, T., Wolff, E., Röthlisberger, R., Mulvaney, R., & Elderfield, H. (2015). Constraints on soluble aerosol iron flux to the Southern Ocean at the Last Glacial Maximum. *Nature Communications*, *6*, 7850.

Dale, A. W., Nickelsen, L., Scholz, F., Hensen, C., Oschlies, A., & Wallmann, K. (2015). A revised global estimate of dissolved iron fluxes from marine sediments. *Global Biogeochemical Cycles*, *29*, 691–707. https://doi.org/10.1002/2014GB005017

Elrod, V. A., Berelson, W. M., Coale, K. H., & Johnson, K. S. (2004). The flux of iron from continental shelf sediments: A missing source for global budgets. *Geophysical Research Letters*, *31*, L12307. https://doi.org/10.1029/2004GL020216

Fennel, K., Abbott, M. R., Spitz, Y. H., Richman, J. G., & Nelson, D. M. (2003). Impacts of iron control on phytoplankton production in the modern and glacial Southern Ocean. *Deep Sea Research Part II*, *50*(3), 833–851.

Franois, R., Altabet, M. A., Yu, E.-F., Sigman, D. M., Bacon, M. P., Frank, M., … Labeyrie, L. D. (1997). Contribution of Southern Ocean surface-water stratification to low atmospheric CO_2 concentrations during the last glacial period. *Nature*, *389*(6654), 929–935.

Galbraith, E. D., Gnanadesikan, A., Dunne, J. P., & Hiscock, M. R. (2010). Regional impacts of iron-light colimitation in a global biogeochemical model. *Biogeosciences*, *7*(3), 1043–1064.

Getzlaff, J., & Dietze, H. (2013). Effects of increased isopycnal diffusivity mimicking the unresolved equatorial intermediate current system in an Earth system climate model. *Geophysical Research Letters*, *40*, 2166–2170. https://doi.org/10.1002/grl.50419

Gledhill, M., & Buck, K. N. (2012). The organic complexation of iron in the marine environment: A review. *Frontiers in Microbiology*, *3*, 69.

Ito, T., & Follows, M. J. (2005). Preformed phosphate, soft tissue pump and atmospheric CO_2. *Journal of Marine Research*, *63*(4), 813–839.

Kalnay, E., Kanamitsu, M., Kistler, R., Collins, W., Deaven, D., Gandin, L., … Dennis, J. (1996). The NCEP/NCAR 40-year reanalysis project. *Bulletin of the American Meteorological Society*, *77*(3), 437–472.

Kohfeld, K. E., Le Quéré, C., Harrison, S. P., & Anderson, R. F. (2005). Role of marine biology in glacial-interglacial CO_2 cycles. *Science*, *308*(5718), 74–78.

Lambeck, K., Rouby, H., Purcell, A., Sun, Y., & Sambridge, M. (2014). Sea level and global ice volumes from the Last Glacial Maximum to the Holocene. *Proceedings of the National Academy of Sciences of the United States of America*, *111*(43), 15,296–15,303.

Lambert, F., Tagliabue, A., Shaffer, G., Lamy, F., Winckler, G., Farias, L., … De Pol-Holz, R. (2015). Dust fluxes and iron fertilization in Holocene and Last Glacial Maximum climates. *Geophysical Research Letters*, *42*, 6014–6023. https://doi.org/10.1002/2015GL064250

Levitus, S., Antonov, J., Baranova, O. K., Boyer, T., Coleman, C., Garcia, H., … Zweng, M. M. (2013). The world ocean database. *Data Science Journal*, *12*, WDS229–WDS234.

Lund, D., Asimow, P., Farley, K., Rooney, T., Seeley, E., Jackson, E., & Durham, Z. (2016). Enhanced east Pacific rise hydrothermal activity during the last two glacial terminations. *Science*, *351*(6272), 478–482.

Luo, C., Mahowald, N., Bond, T., Chuang, P., Artaxo, P., Siefert, R., … Schauer, J. (2008). Combustion iron distribution and deposition. *Global Biogeochemical Cycles*, *22*, GB1012. https://doi.org/10.1029/2007GB002964

Maher, B., Prospero, J., Mackie, D., Gaiero, D., Hesse, P., & Balkanski, Y. (2010). Global connections between aeolian dust, climate and ocean biogeochemistry at the present day and at the Last Glacial Maximum. *Earth-Science Reviews*, *99*(1), 61–97.

Mahowald, N. M., Engelstaedter, S., Luo, C., Sealy, A., Artaxo, P., Benitez-Nelson, C., … Siefert, R. L (2009). Atmospheric iron deposition: Global distribution, variability, and human perturbations*. *Annual Review of Marine Science*, *1*, 245–278.

Marcott, S. A., Bauska, T. K., Buizert, C., Steig, E. J., Rosen, J. L., Cuffey, K. M., … Brook, E. J. (2014). Centennial-scale changes in the global carbon cycle during the last deglaciation. *Nature*, *514*(7524), 616–619.

Martin, J. H. (1990). Glacial-interglacial CO_2 change: The iron hypothesis. *Paleoceanography*, *5*(1), 1–13.

Martínez-García, A., Sigman, D. M., Ren, H., Anderson, R. F., Straub, M., Hodell, D. A., … Haug, G. H. (2014). Iron fertilization of the Subantarctic Ocean during the last Ice Age. *Science*, *343*(6177), 1347–1350.

Meissner, K., Weaver, A., Matthews, H., & Cox, P. (2003). The role of land surface dynamics in glacial inception: A study with the UVic Earth System Model. *Climate Dynamics*, *21*(7–8), 515–537.

Middleton, J. L., Langmuir, C. H., Mukhopadhyay, S., McManus, J. F., & Mitrovica, J. X. (2016). Hydrothermal iron flux variability following rapid sea level changes. *Geophysical Research Letters*, *43*, 3848–3856. https://doi.org/10.1002/2016GL068408

Mongin, M., Nelson, D. M., Pondaven, P., & Tréguer, P. (2007). Potential phytoplankton responses to iron and stratification changes in the Southern Ocean based on a flexible-composition phytoplankton model. *Global Biogeochemical Cycles*, *21*, GB4020. https://doi.org/10.1029/2007GB002972

Moore, J. K., Abbott, M. R., Richman, J. G., & Nelson, D. M. (2000). The Southern Ocean at the Last Glacial Maximum: A strong sink for atmospheric carbon dioxide. *Global Biogeochemical Cycles*, *14*(1), 455–475.

Muglia, J., & Schmittner, A. (2015). Glacial Atlantic overturning increased by wind stress in climate models. *Geophysical Research Letters*, *42*, 9862–9868. https://doi.org/10.1002/2015GL064583

National Geophysical Data Center (2006). 2-minute gridded global relief data (ETOPO2) v2. Boulder, CO: National Geophysical Data Center, NOAA. https://doi.org/10.7289/V5J1012Q

Nickelsen, L. (2015). Modelling the marine biogeochemical implications of aeolian sedimentary and riverine iron supply (PhD thesis), Christian-Albrechts Universität Kiel.

Nickelsen, L., & Oschlies, A. (2015). Enhanced sensitivity of oceanic CO_2 uptake to dust deposition by iron-light colimitation. *Geophysical Research Letters*, *42*, 492–499. https://doi.org/10.1002/2014GL062969

Nickelsen, L., Keller, D., & Oschlies, A. (2015). A dynamic marine iron cycle module coupled to the University of Victoria Earth System Model: the Kiel Marine Biogeochemical Model 2 for UVic 2.9. *Geoscientific Model Development*, *8*, 1357–1381.

Palastanga, V., Slomp, C., & Heinze, C. (2013). Glacial-interglacial variability in ocean oxygen and phosphorus in a global biogeochemical model. *Biogeosciences*, *10*(2), 945–958.

Parekh, P., Follows, M. J., & Boyle, E. (2004). Modeling the global ocean iron cycle. *Global Biogeochemical Cycles*, *18*, GB1002. https://doi.org/10.1029/2003GB002061

Parekh, P., Joos, F., & Mueller, S. A. (2008). A modeling assessment of the interplay between aeolian iron fluxes and iron-binding ligands in controlling carbon dioxide fluctuations during Antarctic warm events. *Paleoceanography*, *23*, PA4202. https://doi.org/10.1029/2007PA001531

Peltier, W., Argus, D., & Drummond, R. (2015). Space geodesy constrains ice age terminal deglaciation: The global ICE-6G_C (VM5a) model. *Journal of Geophysical Research: Solid Earth*, *120*, 450–487. https://doi.org/10.1002/2014JB011176

Resing, J. A., Sedwick, P. N., German, C. R., Jenkins, W. J., Moffett, J. W., Sohst, B. M., & Tagliabue, A. (2015). Basin-scale transport of hydrothermal dissolved metals across the south Pacific Ocean. *Nature*, *523*(7559), 200–203.

Schmittner, A., & Egbert, G. (2013). An improved parameterization of tidal mixing for ocean models. *Geoscientific Model Development*, *6*, 4475–4509.

Schmittner, A., & Somes, C. (2016). Complementary constraints from carbon (^{13}C) and nitrogen (^{15}N) isotopes on the glacial ocean's soft-tissue biological pump. *Paleoceanography*, *31*, 669–693. https://doi.org/10.1002/2015PA002905

Sholkovitz, E. R., Sedwick, P. N., Church, T. M., Baker, A. R., & Powell, C. F. (2012). Fractional solubility of aerosol iron: Synthesis of a global-scale data set. *Geochimica et Cosmochimica Acta*, *89*, 173–189.

Sigman, D. M., & Boyle, E. A. (2000). Glacial/interglacial variations in atmospheric carbon dioxide. *Nature*, *407*(6806), 859–869.

Somes, C. J., & Oschlies, A. (2015). On the influence of "non-Redfield" dissolved organic nutrient dynamics on the spatial distribution of N_2 fixation and the size of the marine fixed nitrogen inventory. *Global Biogeochemical Cycles*, *29*, 973–993. https://doi.org/10.1002/2014GB005050

Somes, C. J., Schmittner, A., Muglia, J., & Oschlies, A. (2017). A three-dimensional model of the marine nitrogen cycle during the Last Glacial Maximum constrained by sedimentary isotopes. *Frontiers in Marine Science*, *4*, 108. https://doi.org/10.3389/fmars.2017.00108

Tagliabue, A., Bopp, L., Roche, D., Bouttes, N., Dutay, J.-C., Alkama, R., … Paillard, D. (2009). Quantifying the roles of ocean circulation and biogeochemistry in governing ocean carbon-13 and atmospheric carbon dioxide at the Last Glacial Maximum. *Climate Past*, *5*(4), 695–706.

Tagliabue, A., Bopp, L., Dutay, J.-C., Bowie, A. R., Chever, F., Jean-Baptiste, P., … Jeandel, C. (2010). Hydrothermal contribution to the oceanic dissolved iron inventory. *Nature Geoscience*, *3*(4), 252–256.

Tagliabue, A., Mtshali, T., Aumont, O., Bowie, A., Klunder, M., Roychoudhury, A., & Swart, S. (2012). A global compilation of dissolved iron measurements: Focus on distributions and processes in the Southern Ocean. *Biogeosciences*, *9*(6), 2333–2349.

Tagliabue, A., Aumont, O., & Bopp, L. (2014). The impact of different external sources of iron on the global carbon cycle. *Geophysical Research Letters*, *41*, 920–926. https://doi.org/10.1002/2013GL059059

Tagliabue, A., Aumont, O., DeAth, R., Dunne, J. P., Dutkiewicz, S., Galbraith, E., … Yool, A. (2016). How well do global ocean biogeochemistry models simulate dissolved iron distributions? *Global Biogeochemical Cycles*, *30*, 149–174. https://doi.org/10.1002/2015GB005289

Tagliabue, A., Bowie, A. R., Boyd, P. W., Buck, K. N., Johnson, K. S., & Saito, M. A. (2017). The integral role of iron in ocean biogeochemistry. *Nature*, *543*(7643), 51–59.

Völker, C., & Tagliabue, A. (2015). Modeling organic iron-binding ligands in a three-dimensional biogeochemical ocean model. *Marine Chemistry*, *173*, 67–77.

Weaver, A. J., Eby, M., Wiebe, E. C., Bitz, C. M., Duffy, P. B., Ewen, T. L., … Yoshimori, M. (2001). The UVic Earth system climate model: Model description, climatology, and applications to past, present and future climates. *Atmosphere-Ocean*, *39*(4), 361–428.

Winton, V., Edwards, R., Delmonte, B., Ellis, A., Andersson, P., Bowie, A., … Tuohy, A. (2016). Multiple sources of soluble atmospheric iron to Antarctic waters. *Global Biogeochemical Cycles*, *30*, 421–437. https://doi.org/10.1002/2015GB005265